Journal of
Materials Chemistry A

Materials for energy and sustainability

rsc.li/materials-a
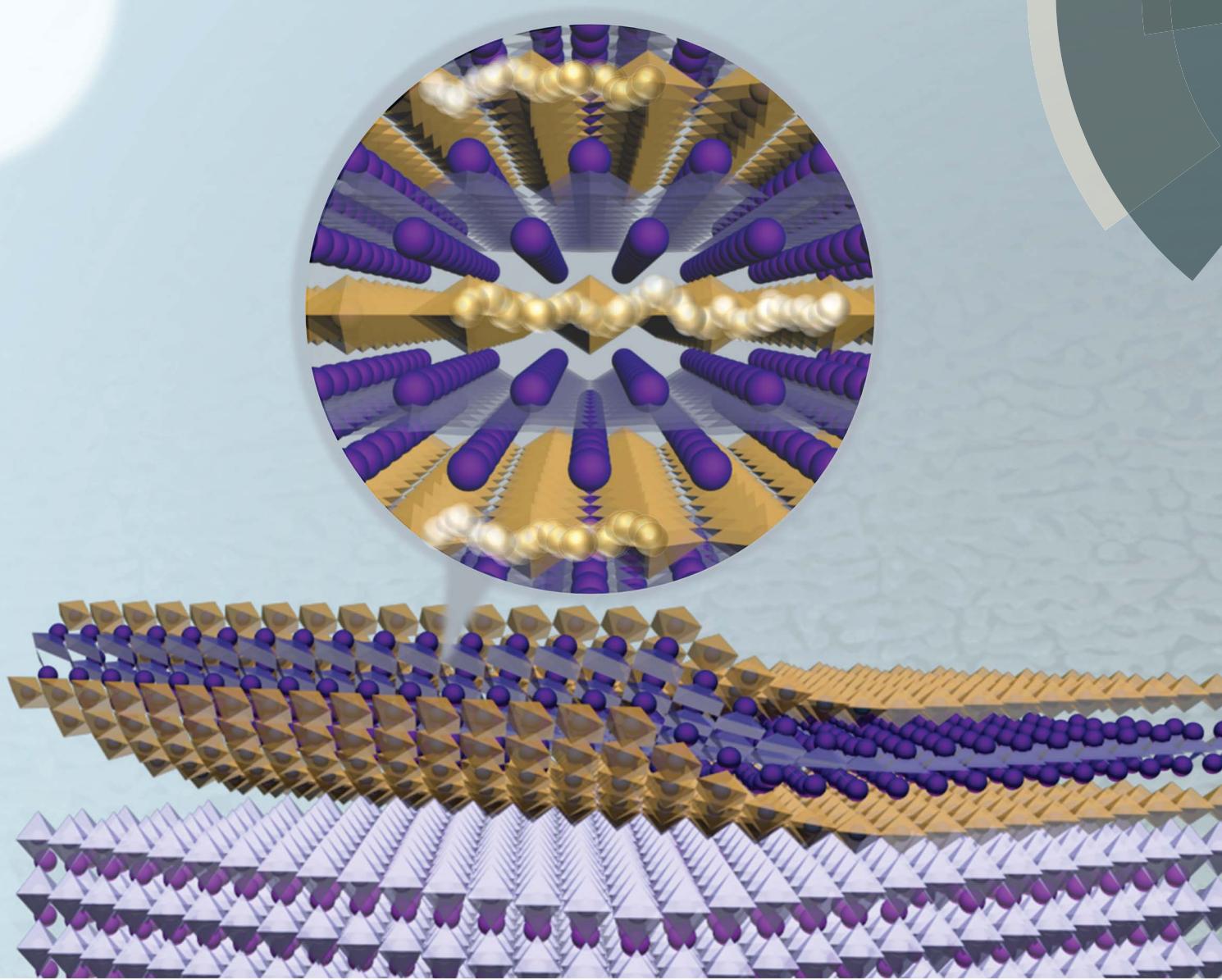
ROYAL SOCIETY OF CHEMISTRY | Celebrating IYPT 2019

COMMUNICATION
Albert Tarancón *et al.*
Thin film oxide-ion conducting electrolyte for near room
temperature applications

COMMUNICATION

Check for updates

Thin film oxide-ion conducting electrolyte for near room temperature applications†

Iñigo Garbayo, ‡[a] Francesco Chiabrera, [a] Nerea Alayo, [a] José Santiso, [b] Alex Morata [a] and Albert Tarancón *[ac]

Stabilized bismuth vanadate thin films are presented here as superior oxide ionic conductors, for application in solid state electrochemical devices operating near room temperature. Widely studied in the 90s in bulk form due to their unbeatable ionic conduction, this family of materials was finally discarded due to poor stability above 500 °C. Here, we however unveil the possibility of using $Bi_4V_{1.8}Cu_{0.2}O_{10.7}$ at reduced temperatures in thin film-based devices, where the material keeps its unmatched conduction properties and at the same time shows good stability over a wide oxygen partial pressure range.

The quest for high oxygen ion ceramic conductors has been a very active field of research for decades.[1] Aiming to reduce the operating temperature of different oxide ion-driven solid state devices such as solid oxide fuel cells (SOFC) or oxygen sensors, it became necessary to look for alternatives to the state-of-the-art yttria-stabilized zirconia (YSZ) electrolyte material.[2–5] The sluggish ion hopping of YSZ typically limited the device operation of bulk systems to *e.g.* 800 °C in the case of SOFCs,[1] or 450 °C for oxygen sensors.[6] With the standardization of thin film deposition techniques in the last decades, a significant lowering of the device operating temperature could be attained, simply derived from a substantial reduction of the electrolyte thickness (around 3 orders of magnitude, down to the sub-micrometre range).[7] The use of oxide thin films gave rise to new families of integrated solid state MicroElectroMechanical System (MEMS) devices operating at intermediate temperatures, such as thin film SOFCs (TF-SOFCs) for portable power applications,[8–10] micro sensors for integrated sensing networks,[11,12] or resistive switching devices for data processing.[13–15]

In the case of TF-SOFCs, the use of hundreds of nanometres thick YSZ electrolytes set a new minimum operating temperature at *ca.* 450 °C.[16–18] When compared to the typical bulk SOFC working temperatures, such a reduction in temperature undoubtedly meant a significant technological breakthrough, attaining quick and low power consuming start-up processes. However, the new temperature range still entailed important restrictions to the cell performance of TF-SOFCs. First, an operating temperature of ~450 °C was incompatible with state-of-the-art SOFC ceramic electrodes,[19] limiting the portfolio of possible electrode materials to inherently instable porous metallic films.[8,17,18,20,21] Also, the integration of TF-SOFCs with additional components of the final portable powering device (reformers, post-combustors, or simply electronics)[22,23] required a full integration of the system microfabrication in CMOS-compatible Si technology, typically restricted to maximum peak temperatures of 450 °C.[24] This limited the broad implementation of TF-SOFC (and, for similar reasons, also gas microsensors) from both a materials and a microfabrication point of view. Further lowering of the operating temperature is therefore still required, for which we are entailed to look for alternative high oxygen conducting electrolyte materials able to operate at reduced temperatures, eventually room temperature.

Low temperature operating oxide ionic conductors find important applications as well in the emerging data storage devices based on transition metal oxide electronic systems, *via* resistive switching,[15] electronic phase transitions[25] or voltage controlled ion gating.[26] In this sense, it is of particular interest to this work a recent pioneering paper from Yildiz and co-workers, who showed that electrochemically driven phase changes in oxide materials (in particular, V_xO_y) can be used to trigger metal-insulator transitions and, thus, force large changes in resistivity that could be used for data storage.[27] In such system, an ionic conductor is used as gating material, pumping oxygen to (or pulling it out from) the oxide working

aDepartment of Advanced Materials for Energy Applications, Catalonia Institute for Energy Research (IREC), Jardins de les Dones de Negre 1, 08930 Sant Adrià del Besòs, Barcelona, Spain. E-mail: atarancon@irec.cat

bCatalan Institute of Nanoscience and Nanotechnology (ICN2), CSIC, Barcelona Institute of Science and Technology, Campus UAB, Bellaterra, Barcelona, 08193, Spain

cICREA, Passeig Lluís Companys 23, 08010, Barcelona, Spain

25772 | *J. Mater. Chem. A*, 2019, 7, 25772–25778

This journal is © The Royal Society of Chemistry 2019

electrode, forcing the phase change. However, high oxygen mobility needed in the gate limited the operation with solid state materials (YSZ) to a minimum temperature of 300 °C, while room temperature operation was only achieved using ionic liquid gates. Solid state gate materials with superior oxide ionic conduction can therefore open interesting opportunities for the fabrication of electrochemically driven, room temperature operating compact all-solid state memories.

Clearly, the number of alternatives to YSZ is very limited, and all come at a cost. Materials with higher ionic conductivity than YSZ at intermediate temperatures usually suffer from fast degradation under reducing conditions, see *e.g.* ceria-based electrolytes at $T > 600$ °C.[1] Among the explored alternatives, it is to be highlighted the BIMEVOX family, as the electrolyte material with the highest ionic conductivity at intermediate temperatures ever reported. Firstly described in 1990 by Abraham *et al.*,[28] BIMEVOX presents a layered aurivillius structure consisting of alternating $\{Bi_2O_2\}^{2+}$ and transition metal-doped perovskite $\{VO_{3.5}\square_{0.5}\}^{2-}$ layers, see Fig. 1a. The high presence of disordered oxygen vacancies in the perovskite sheets is the responsible for the high oxygen mobility, which is maximized when stabilizing the tetragonal γ-phase. In the undoped parent compound $Bi_4V_2O_{11}$, temperatures below 550 °C lead to the formation of additional monoclinic α and orthorhombic β phases with lower conductivity;[29] however,

doping with different transition metals has been proved to successfully stabilize the γ-phase down to room temperature. Among the different options, BICUVOX (which stands for the corresponding BIMEVOX doped with Cu and formula $Bi_4V_{1.8}Cu_{0.2}O_{10.7}$, for a typical 10 mol% doping) was shown to present the highest ionic conductivity.[28] However, a non-trivial electronic conductivity already at intermediate temperatures ($T \sim 500$ °C),[30] irreversible phase changes under reducing atmospheres[31] and a high thermal expansion coefficient[32] drastically hindered the broad application of this material (and the rest of BIMEVOXes) in final pellet-based SOFCs, operating in the intermediate-temperature range. Consequence of this, the material was practically abandoned by the end of that decade, except for its use in oxygen separation membranes.[33,34]

However, the possibility of fabricating thin film devices, in which the operating temperature can be significantly lowered, opens the door to explore such an outstanding material in a new low temperature range ($T \ll 500$ °C), where the chemical instability is expected to be significantly hindered. Despite the promising possibilities for low temperature applications, three decades after the discovery of the high ionic conductivity of BIMEVOX only a few works have dealt with the thin film deposition of this material (thickness <500 nm and low temperature processing),[35,36] and a study of its electrochemical performance at this temperature range is still lacking. In this
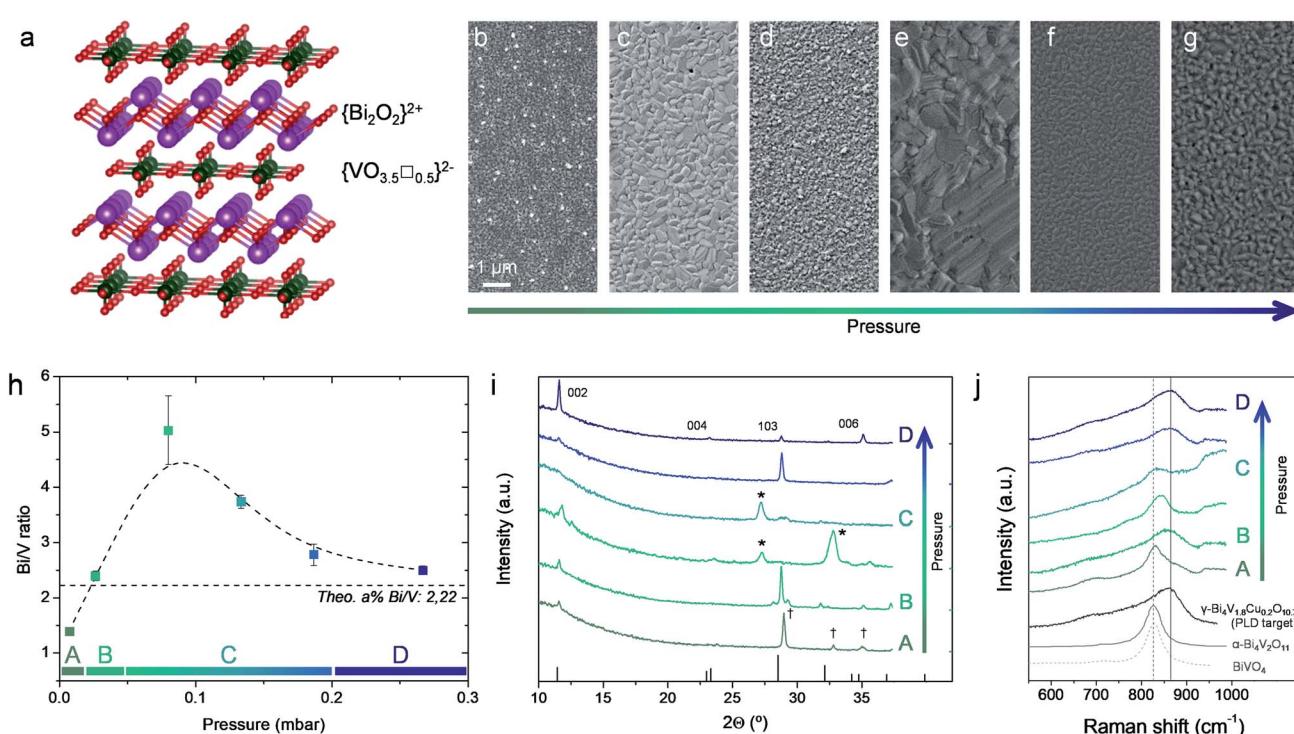
Fig. 1 (a) Atomic representation of the γ-$Bi_4V_2O_{11}$ aurivillius layered structure (drawings produced by VESTA 3 software).[50] (b–g) Top view SEM images of representative films deposited by PLD at different background pressures ($p = 0.0067–0.267$ mbar) and a constant target-to-substrate distance of 11 cm, on top of Si substrates. (h) Bi/V ratio as a function of deposition pressure. Dashed line is included as guide for the eyes. Four different pressure regions are identified (A–D) (i) X-ray diffractogram obtained for the same BICUVOX film series. Main diffractions of the γ-$Bi_4V_2O_{11}$ phase are indicated (ICDD reference code 00-048-0273), as well as the appearance of secondary phases (Bi_2O_3 *, $BiVO_4$ †) (j) Raman spectra of the BICUVOX film series, plus references for γ-$Bi_4V_{1.8}Cu_{0.2}O_{10.7}$ (measured on the pellet used as PLD target),[42] α-$Bi_4V_2O_{11}$ (ref. 43) and $BiVO_4$.[41]
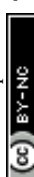
work, we optimized the deposition of BICUVOX thin films by means of Pulsed Laser Deposition (PLD) and we studied its electrochemical performance at $T = 50$–$450\ ^{\circ}$C. First, we extend previous works and show the tremendous capabilities of PLD for tuning the stoichiometry in this type of films, simply changing the deposition conditions. Then, we present the conduction properties of the optimized BICUVOX films, by measuring its oxygen conductivity as a function of temperature. Noting the layered crystal structure of BICUVOX with oxide ionic diffusion taking place mainly along the $\{VO_{3.5}\square_{0.5}\}^{2-}$ layers, we investigated the anisotropy in the conduction by preparing epitaxial films and measuring their conductivity in orthogonal directions (parallel and perpendicular to the perovskite sheets).

The optimization of PLD deposition of BICUVOX thin films was carried out by preparing a set of polycrystalline films (thickness ranging from 100 to 300 nm) under varying depositing conditions, *viz.* background oxygen pressure (p) and target-to-substrate distance (d). Other parameters such as deposition temperature and laser fluence were previously optimized for obtaining homogeneous crystalline films and then intentionally set constant, at 600 $^{\circ}$C and 0.45 J cm^{-2} respectively. Thin films were grown from a home-made $Bi_4V_{1.8}Cu_{0.2}O_{10.7}$ target, p was varied from 0.0067 to 0.267 mbar and two target-to-substrate distances were studied, $d = 9$ and 11 cm (note the longer distances typically used in our large area PLD system compared to "standard" research-scale PLD systems; more details in the Experimental section).[37] Dense films were obtained within the whole experimental window of pressures and distances, with considerable variations in the grain size (see representative top view Scanning Electron Microscopy (SEM) images in Fig. 1b–g, for selected background oxygen pressures and $d = 11$ cm; corresponding images for $d = 90$ mm can be found in the ESI, Fig. S1†). A stoichiometric analysis of the deposited films was then carried out by Energy-Dispersive X-ray spectroscopy (EDX), Fig. 1h and S2† (specific films were also measured by Wavelength Dispersive Spectroscopy, WDS, confirming the trends). We observed an evolution of the cationic ratio Bi/V as a function of the pressure in analogy with similar representations in the literature involving depositions of heavy *vs.* light elements (H/L) by PLD.[38] We differentiate four different regions; a first region A for low p below 0.0267 mbar, where Bi deficient films are obtained; a region B ($p \approx 0.0267$ mbar), where a good stoichiometry is maintained; a region of intermediate pressures C ($0.0267 < p < 0.187$ mbar) in which an important V deficiency is observed; and a final region D at higher pressures ($p > 0.187$ mbar), where the film approaches again the target stoichiometry. The observed trend matches well with the expected plume dynamics as a function of the background pressure.[38,39] In short, at lower background pressures weak scattering is expected in the laser plume for all the species independently on their size, so the stoichiometry can be well maintained. With increasing pressure, scattering is expected to affect greater to the lighter species (V in our case), giving rise to off-stoichiometric films (light element-deficient). If we keep increasing the background pressure, heavy elements (Bi) start to scatter as well and the plume ends up in a diffusion front in which the correct

stoichiometry is recovered, and thus in the films (region D). The presence of a Bi-deficient region at the lowest deposition pressure (region A) is probably related to the high volatility of Bi, which would provoke that at low background pressures, where no collisions are expected in the plume, Bi simply flies away.[40] In our case, two pressure regions are clearly identified as preferred for obtaining stoichiometric BICUVOX films, regions B ($p = 0.0267$ mbar) and D ($p > 0.187$ mbar).

Importantly, no clear trend could be detected for Cu with the background pressure. However, important differences were detected between the different deposition pressure regions. First, in the low pressure regimes A and B, $p = 0.0067$–0.0267 mbar, we could identify the presence of homogeneously distributed Cu-rich micrometre-size particles (probably CuO), see top-view SEM image in Fig. S3.† At the same time, in this range it was impossible to detect Cu out of these particles (*i.e.* in the film), suggesting that Cu could not be successfully integrated in the material and that the films deposited at low p are composed by undoped $Bi_4V_2O_{11}$. Opposed to that, for $p > 0.0267$ mbar (regions C and D), Cu was detected all along the films in the right proportion and no particles were observed. This suggests that in these regimes Cu is indeed successfully incorporated in the BICUVOX structure of the films.

X-Ray Diffraction (XRD) and Raman spectroscopy were carried out in order to analyse the phase evolution through the film series, and the correlation between Bi/V ratio and phase stabilization (Fig. 1i and j). Indeed, the appearance of expectable secondary phases is clearly observed in the films with stoichiometry distant from the targeted one. Analysing the XRD pattern in Fig. 1i, one can observe: (i) the appearance of a Bi-deficient $BiVO_4$ phase at low deposition pressures ($p < 0.0267$ mbar, region A), probably a mix of clinobisvanite and dreyerite phases,[41] and (ii) the presence of Bi_2O_3 in the V-deficient region C, $0.0267 < p < 0.187$ mbar (peaks marked as *). Moreover, even though the desired stoichiometry was measured in films deposited in region B, XRD revealed the presence of additional reflections (see *e.g.* the triplet peak at $2\theta \approx 28^{\circ}$), presumably due to the aforementioned non-incorporation of Cu in the aurivillius structure and a subsequent non-stabilization of the tetragonal γ-phase. Contrary, at the highest deposition pressures, $p > 0.187$ mbar, single γ-$Bi_4V_{1.8}Cu_{0.2}O_{10.7}$ phase could only be detected.

Similar conclusions can be drawn by Raman spectroscopy, Fig. 1j. In fact, it is to be highlighted the goodness of Raman spectroscopy for identifying phase formation in the $Bi_4V_2O_{11}$ family, since a clear shift in wavenumber, from $\sim$860 cm^{-1} to $\sim$830 cm^{-1}, happens when moving from the tetragonal γ-phase to monoclinic α-phase (see difference between the γ-$Bi_4V_{1.8}$-$Cu_{0.2}O_{10.7}$, measured in the pellet used as PLD target and perfectly matching previous reports,[42] and the α-$Bi_4V_2O_{11}$ from ref. 43). This way, we could clearly identify the presence of the desired tetragonal phase in the films deposited at high pressure, region D ($p > 0.187$ mbar). Meanwhile, α-$Bi_4V_2O_{11}$ was detected in the intermediate pressures, and $BiVO_4$ was presumably measured at the lowest pressure tested (note here that similar spectra have been reported for both α-$Bi_4V_2O_{11}$ and $BiVO_4$, making impossible to differentiate them by this

25774 | *J. Mater. Chem. A*, 2019, **7**, 25772–25778

This journal is © The Royal Society of Chemistry 2019

technique). Surprisingly, at $p \approx 0.0267$ mbar Raman spectroscopy also shows the stabilization of the γ-phase, even though Cu is apparently not well incorporated in the structure. Still, we can conclude that XRD and Raman results fully support, from a structural point of view, the stoichiometric evolution previously observed, and suggest the need of high background pressures of $p > 0.187$ mbar for the stabilization of the aurivillius BICUVOX γ-phase.

Based on this, we additionally prepared epitaxial BICUVOX films grown on (001)-oriented $SrTiO_3$ substrates (undoped – STO and doped with 1.0 at% Nb – Nb:STO), at the optimum deposition pressure of $p = 0.267$ mbar. Fig. 2a shows a representative XRD pattern of a 36 nm-thick BICUVOX film deposited on Nb:STO (see section S2 of the ESI† for the corresponding measurements on undoped STO). The appearance of a set of reflections corresponding to the (00L) family of planes reveals a perfect epitaxial growth of the tetragonal aurivillius γ-phase, (00L)-oriented in the c-axis (more details in section S2†). The φ-scan presented in the inset of Fig. 2a confirms a cube-on-cube growth of the tetragonal BICUVOX on top of Nb:STO with perfect match of the (100) planes of both materials, see schematics in Fig. 2c. Note the almost identical in-plane lattice parameter of BICUVOX, $a_{BICUVOX} = 3.907$ Å,[28] as compared to the cubic STO, $a_{STO} = 3.905$ Å, meaning a lattice mismatch of only +0.05%. The epitaxy was confirmed by performing high resolution XRD reciprocal space maps (RSM), Fig. 2b and S4.† The figure shows the coexisting reflections (-103) of the Nb:STO and (-1011) of the BICUVOX, revealing a perfect in-plane matching thanks to the very similar in-plane lattice parameters.

Furthermore, the quality of the films was analysed by top-view non-contact AFM images, Fig. 2d and e. The images showed a clear formation of terraces, typical of layer by layer growth,[35] and a complete absence of significant defects or particulates in the top surface. The height profile obtained along the top surface (black dashed arrow in Fig. 2e) revealed very small steps of ~3.5 Å, see Fig. 2f. These steps are clearly smaller than the out-of-plane lattice parameter ($c_{BICUVOX} = 15.44$ Å, as calculated from the out-of-plane XRD pattern and matching previous literature).[28] We speculate that these steps correspond to single $\{Bi_2O_2\}^{2+}$ or $\{VO_{3.5}\square_{0.5}\}^{2-}$ sub-layers, 4 every unit cell, thus matching the obtained average value. In conclusion, we were able to grow high quality epitaxial BICUVOX films in two functional substrates, one dielectric (STO), one conductive (Nb:STO), ideal for further electrochemical analysis.

Ionic conductivity in the whole set of BICUVOX films was investigated by means of Electrochemical Impedance Analysis (EIS). Epitaxial (on STO-based substrates) and polycrystalline (on $Si_3N_4/SiO_2/Si$ substrates) films were measured in a temperature range from 50 to 450 °C, under ambient conditions (corresponding Nyquist plots can be found in the ESI, Fig. S6†). First, the effect of film off-stoichiometry and presence of secondary phases (see Fig. 1) on the conduction properties of the polycrystalline films was confirmed, correlating the stabilization of the fast conducting and stable γ-phase with the obtaining of highest (and stable) conductivity (see section S3 in
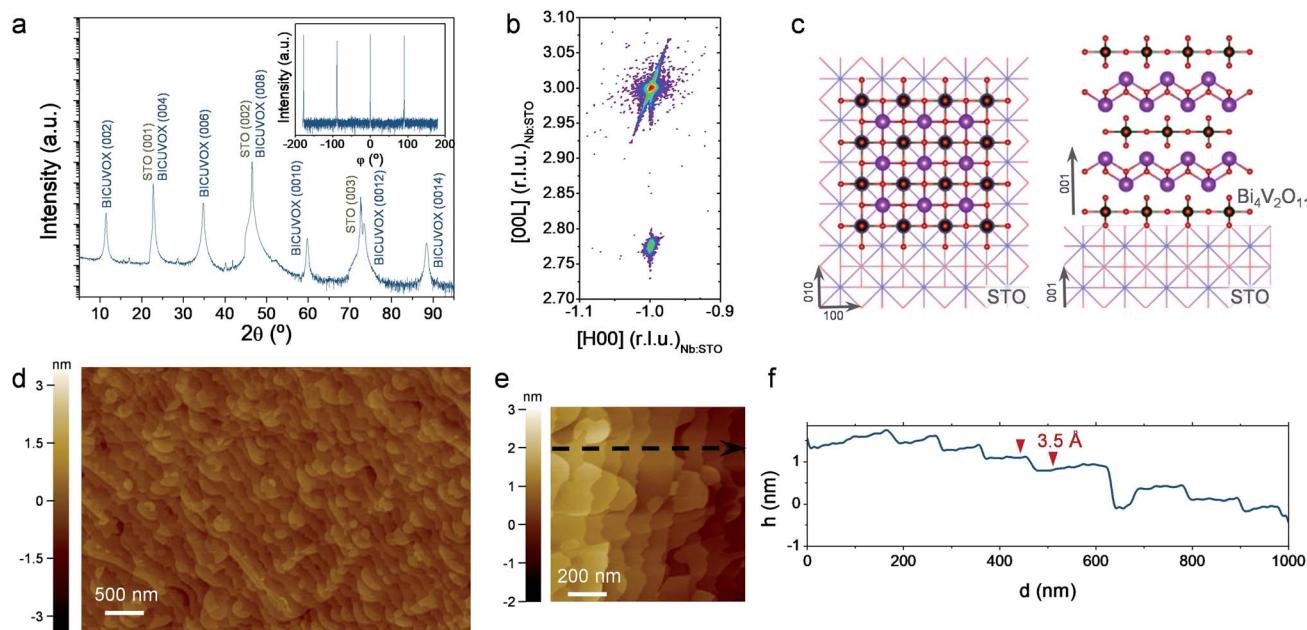
Fig. 2 (a and b) X-ray diffraction patterns of a 36 nm thick BICUVOX film deposited on Nb-doped $SrTiO_3$. (a) Out-of-plane $\theta-2\theta$ X-ray diffraction pattern, where the set of peaks corresponding to the 00L reflections is visible. A φ scan around the (-103) reflection of $SrTiO_3$ is also included in the inset, showing a 4-fold symmetry corresponding to a single in-plane orientation (100) BICUVOX/(100) $SrTiO_3$. (b) Shows the in-plane Reciprocal Space Map around the -103 reflection peak of the Nb-doped $SrTiO_3$ substrate. (c) Schematic representations of the epitaxial growth of γ-$Bi_4V_2O_{11}$ on top of 001-oriented $SrTiO_3$ single crystals, top and cross-sectional views. (d and e) AFM images of an epitaxial BICUVOX film grown on top of Nb-doped $SrTiO_3$, with two different magnifications. (f) Height profile corresponding to the black dashed arrow shown in figure (e). The average step height is shown as well (only single step terraces are considered for the average calculation).

This journal is © The Royal Society of Chemistry 2019

J. Mater. Chem. A, 2019, **7**, 25772–25778 | **25775**

the ESI†). We then focus on the analysis of the polycrystalline *vs.* epitaxial films, all deposited at the optimum pressure range, $p = 0.267$ mbar. Fig. 3a presents the Arrhenius representation of the conductivity evolution with temperature, for one polycrystalline film and two epitaxial BICUVOX films measured at two different configurations, *viz.* in-plane (on STO) and cross-plane (on Nb:STO), using top Au electrodes (further details on the different measuring configurations can be found in section S3†). The obtained results are compared with reference bulk polycrystalline BICUVOX, as well as single crystal BICUVOX in two directions (parallel and perpendicular to the $(100)_{BICUVOX}$ planes) and, finally, YSZ and Gd-doped CeO_2 (CGO) thin film conductivity.[16,47–49]

Although significant differences are found among the different films, all present an improvement in terms of ionic

Fig. 3 (a) Arrhenius representation of the evolution of ionic conductivity for different BICUVOX (polycrystalline, epitaxial) films with temperature, all deposited at $p = 0.267$ mbar. References for bulk polycrystalline BICUVOX,[28] single crystal BICUVOX (parallel and perpendicular to the $(100)_{BICUVOX}$ planes),[48] YSZ thin film[16,46] and CGO thin film[44,45] are included for comparison. Inset schematics show the direction of oxygen mobility in the two measuring configurations, for the epitaxial films. Activation energies (E_a) are also indicated for the measured films. (b) pO_2 dependence of BICUVOX in-plane conductivity, measured in an epitaxial film at different temperatures ($T = 150–350$ °C) and in a polycrystalline sample at $T = 250$ °C. Oxygen partial pressure is measured by an oxygen sensor at the outlet of the gases. Dashed lines are included as guide for the eyes.

conduction *vs.* state-of-the-art YSZ and CGO, especially when reducing temperature (due to the lower activation energies, E_a). The highest conductivity is clearly obtained in the epitaxial BICUVOX film when measuring in-plane, followed by the polycrystalline film and, finally, the epitaxial measured cross-plane. As for the activation energies, one single mechanism could be observed for the whole range of measuring temperatures, with slightly higher E_a for the cross-plane than for the in-plane conduction.

The measured in-plane conductivity for the epitaxial film goes in line with literature values for bulk BICUVOX, confirming the outstanding oxide ionic conductivity of this material in thin film form (the slightly higher E_a values could be related to the plausible presence of structural defects in the films or small off-stoichiometries). The expected anisotropy in the conduction, depending on the oxygen hopping direction, is also clearly observed in the measured films, with more than two orders of magnitude higher in-plane conductivity than cross-plane. Similar anisotropy was previously reported in single crystal BICUVOX and matches well with our XRD results, Fig. 2, since enhanced oxygen mobility in BICUVOX is known to happen along the $\{VO_{3.5}\square_{0.5}\}^{2-}$ sub-layers, *i.e.* in the direction parallel to the substrate surface (in-plane), and hindered when crossing the $\{Bi_2O_2\}^{2+}$ sub-layers, *i.e.* in the $(001)_{BICUVOX}$ direction, across the film.[48,50] Interestingly, the polycrystalline film presents both an intermediate conductivity and activation energy, probably derived from the random orientation of the grains and the presence of grain boundaries.

Notably, these results position the prepared epitaxial BICUVOX films as the thin film material with highest (in-plane) ionic conductivity ever reported for low temperature applications ($T < 300$ °C), with important implications for their application in advanced thin film-based devices. However, apart from the outstanding oxide ionic conductivity, low temperature operation with BICUVOX films also requires high stability in a wide range of pO_2, from oxidizing to highly reducing atmospheres (especially for applications in powering devices). Indeed, as commented before, this has been the main drawback of BICUVOX hindering its use as electrolyte material at higher temperatures in the past. We therefore studied the stability *vs.* pO_2 of the utmost performing BICUVOX epitaxial film in its new operating temperature range, $T < 300$ °C. Fig. 3b presents the in-plane conductivity measured by EIS at different temperatures, from 150 °C to 350 °C, and oxygen partial pressures, from $pO_2 = 0.21$ bar (synthetic air) to $pO_2 = 10^{-19}$ bar (5 vol% H_2 in Ar). For temperatures below 300 °C, the figure shows great stability (flat profiles) within the whole range of pO_2 (from oxidizing to highly reducing conditions), proving the effectiveness of the material to be used in thin film-based low temperature operating devices. The maximum operating temperature for epitaxial BICUVOX is set in this study at $T = 350$ °C, since a clear effect on the conductivity is observed there when reducing pO_2. It is important to note, though, that the observed trend at this temperature matches well with an unexpected p-type conduction behaviour. The appearance of this conduction comportment at this temperature requires attention and will be a matter of discussion in further works.

25776 | *J. Mater. Chem. A*, 2019, **7**, 25772–25778

This journal is © The Royal Society of Chemistry 2019

Finally, we also analysed the stability *vs.* pO_2 of the BICUVOX polycrystalline films. Although not as outstanding as the in-plane conductivity measured in the epitaxial films (between one and two orders of magnitude lower), the polycrystalline BICUVOX already represents an important reduction of ~150 °C and ~100 °C *vs.* YSZ and CGO respectively, with a potential operating temperature below 300 °C. As shown in Fig. 3b stability tests (open symbols), negligible conductivity changes *vs.* pO_2 were detected also in the polycrystalline films at $T = 250$ °C, thus proving the viability of the material in the low temperature operating range. Taking into account that for certain applications this microstructure might be significantly easier to implement than an epitaxial film (*e.g.* in the already existing TF-SOFC systems), polycrystalline BICUVOX are expected to play a crucial role in future low temperature devices too.

Conclusions

Epitaxial and polycrystalline BICUVOX thin films are presented here as superior oxygen conducting electrolyte materials, for their application in thin film-based low temperature operating electrochemical solid state devices. The highest conductivity was observed in the epitaxial BICUVOX films when measuring parallel to the $\{VO_{3.5}\square_{0.5}\}^{2-}$ planes, matching that previously reported for bulk BICUVOX and thus surpassing any other thin film oxide ion conducting material ever reported at the low temperature operating range ($T < 300$ °C). At the same time, polycrystalline BICU-VOX films also showed an outstanding performance, with forecasted operating temperature below 300 °C. The high ionic conductivity, added to the high stability *vs.* pO_2 proved in this low temperature range, anticipates the potential use of BICUVOX down to room temperature in a new family of non-heated solid state electrochemical systems. Importantly, the use of this material opens up amazing possibilities for the fabrication of solid state devices fully integrated in CMOS processing technologies and with possible encapsulation in plastics.

Experimental section

Thin film deposition by PLD

BICUVOX thin films were deposited by large-area pulsed laser deposition (PLD5000, PVD Products) under different background O_2 pressures (0.0067 to 0.267 mbar) and target-to-substrate distances (9 to 11 cm), from a home-made $Bi_4V_{1.8}$-$Cu_{0.2}O_{10.7}$ pellet target. For the fabrication of the target, Bi_4-$V_{1.8}Cu_{0.2}O_{10.7}$ powder was first synthesized in-house by solid state synthesis, from the basic oxide precursors (Bi_2O_3, V_2O_5 and CuO) mixed in the right stoichiometric proportion. Then, a 3″ pellet was pressed by uniaxial pressing and sintered under ambient air at 850 °C for 6 h. All BICUVOX films were deposited at a substrate temperature of 600 °C, and on various types of substrates, including single crystal Si (100-oriented), sapphire, fused silica, and Si (100) coated with Si_3N_4 (300 nm)/SiO_2 (100 nm) dielectric bilayer. For the growth of epitaxial BICUVOX films, $SrTiO_3$ (STO) and Nb-doped STO (Nb:STO) substrates (Crystal GmbH, Germany) were used, for in-plane and cross-plane electrochemical analysis, respectively.

Thin film structural and compositional characterization

Long range crystalline structure of the deposited films was characterized by X-ray Diffraction (XRD, Bruker D8 Advanced), under a typical $\theta/2\theta$ Bragg–Brentano geometry. For the epitaxial films, a four-angle diffractometer (X'Pert MRD-Panalytical) was used with a Cu Kα radiation source. Additionally, the near range order was analysed by Raman spectroscopy (Horiba Jobin Ybon iHR320). For the Raman measurements, green laser ($\lambda = 532$ nm) was utilized under no light polarization. Thin films microstructure was studied by Scanning Electron Microscopy top view imaging (SEM, ZEISS AURIGA). SEM-coupled Energy-Dispersive X-ray spectroscopy (EDX) was used for the elemental distribution analysis. Errors in the EDX analysis were estimated by calculating the standard deviation from multiple measurements in several samples. Non-contact Atomic Force Microscopy (AFM, XE 100 Park System Corp.) was additionally used for top view imaging of the epitaxial BICUVOX films.

Thin film electrochemical measurements

Electrochemical Impedance Spectroscopy (EIS) was used for measuring the electrical properties of the BICUVOX films, with the help of a Novocontrol Alpha-A Impedance analyser. 100 nm-thick top Au blocking interdigitated (for in-plane measurements) and circular (for cross-plane measurements) electrodes with varying sizes were first defined by photolithography and then deposited by e-beam evaporation (OERLIKON UNIVEX 450B). Impedance was measured in a frequency range of 1 MHz–0.1 Hz applying an AC voltage of 50 mV, in a temperature-controlled Linkam probe station, from 50 to 450 °C. Results were analysed with a ZView software and fitting was carried out applying equivalent circuit modelling.

Conflicts of interest

There are no conflicts to declare.

Acknowledgements

References

1 J. B. Goodenough, *Annu. Rev. Mater. Res.*, 2003, **33**, 91–128.
2 S. C. Singhal and K. Kendall, *High Temperature Solid Oxide Fuel Cells: Fundamentals, Design, and Applications*, Elsevier Advanced Technology, 2003.
3 A. Tarancón, *Energies*, 2009, **2**, 1130–1150.
4 Z. Gao, L. V. Mogni, E. C. Miller, J. G. Railsback, S. A. Barnett, J. B. Goodenough, K. Huang, A. Tarancon, H. Yokokawa, J. Janek, Y. Shao-Horn, J. H. Lang, J. H. Yang, T. McColm, R. Trezona, A. Selcuk, M. Schmidt and L. Verdugo, *Energy Environ. Sci.*, 2016, **9**, 1602–1644.

This journal is © The Royal Society of Chemistry 2019

J. Mater. Chem. A, 2019, **7**, 25772–25778 | **25777**

5 B. Singh, S. Ghosh, S. Aich and B. Roy, *J. Power Sources*, 2017, **339**, 103–135.

6 A. M. Azad, S. A. Akbar, S. G. Mhaisalkar, L. D. Birkefeld and K. S. Goto, *J. Electrochem. Soc.*, 1992, **139**, 3690.

7 D. Beckel, A. Bieberle-Hütter, A. Harvey, A. Infortuna, U. P. Muecke, M. Prestat, J. L. M. Rupp and L. J. Gauckler, *J. Power Sources*, 2007, **173**, 325–345.

8 M. Tsuchiya, B.-K. Lai and S. Ramanathan, *Nat. Nanotechnol.*, 2011, **6**, 282–286.

9 A. Evans, A. Bieberle-Hütter, J. L. M. Rupp and L. J. Gauckler, *J. Power Sources*, 2009, **194**, 119–129.

10 I. Garbayo, D. Pla, A. Morata, L. Fonseca, N. Sabaté and A. Tarancón, *Energy Environ. Sci.*, 2014, **7**, 3617–3629.

11 B.-U. Moon, J.-M. Lee, C.-H. Shim, M.-B. Lee, J.-H. Lee, D.-D. Lee and J.-H. Lee, *Sens. Actuators, B*, 2005, **108**, 271–277.

12 S. Yu, Q. Wu, M. Tabib-Azar and C.-C. Liu, *Sens. Actuators, B*, 2002, **85**, 212–218.

13 R. Waser and M. Aono, *Nat. Mater.*, 2007, **6**, 833–840.

14 D. Ielmini, *Semicond. Sci. Technol.*, 2016, **31**, 063002.

15 C. Bäumer and R. Dittmann, in *Metal Oxide-Based Thin Film Structures*, Elsevier, 2018, pp. 489–522.

16 I. Garbayo, A. Tarancón, J. Santiso, F. Peiró, E. Alarcón-LLadó, A. Cavallaro, I. Gràcia, C. Cané and N. Sabaté, *Solid State Ionics*, 2010, **181**, 322–331.

17 K. Kerman, B.-K. Lai and S. Ramanathan, *J. Power Sources*, 2011, **196**, 2608–2614.

18 J. An, Y.-B. Kim, J. Park, T. M. Gür and F. B. Prinz, *Nano Lett.*, 2013, **13**, 4551–4555.

19 I. Garbayo, V. Esposito, S. Sanna, A. Morata, D. Pla, L. Fonseca, N. Sabaté and A. Tarancón, *J. Power Sources*, 2014, **248**, 1042–1049.

20 K. Kerman, B.-K. Lai and S. Ramanathan, *J. Power Sources*, 2012, **202**, 120–125.

21 Y. Takagi, S. Adam and S. Ramanathan, *J. Power Sources*, 2012, **217**, 543–553.

22 D. Pla, A. Sánchez-González, I. Garbayo, M. Salleras, A. Morata and A. Tarancón, *J. Power Sources*, 2015, **293**, 264–273.

23 B. Scherrer, A. Evans, A. J. Santis-Alvarez, B. Jiang, J. Martynczuk, H. Galinski, M. Nabavi, M. Prestat, R. Tölke, A. Bieberle-Hütter, D. Poulikakos, P. Muralt, P. Niedermann, A. Dommann, T. Maeder, P. Heeb, V. Straessle, C. Muller and L. J. Gauckler, *J. Power Sources*, 2014, **258**, 434–440.

24 S. Sedky, A. Witvrouw, H. Bender and K. Baert, *IEEE Trans. Electron Devices*, 2001, **48**, 377–385.

25 N. Shukla, A. V. Thathachary, A. Agrawal, H. Paik, A. Aziz, D. G. Schlom, S. K. Gupta, R. Engel-Herbert and S. Datta, *Nat. Commun.*, 2015, **6**, 7812.

26 A. L. Krick and S. J. May, *APL Mater.*, 2017, **5**, 042504.

27 Q. Lu, S. R. Bishop, D. Lee, S. Lee, H. Bluhm, H. L. Tuller, H. N. Lee and B. Yildiz, *Adv. Funct. Mater.*, 2018, **28**, 1803024.

28 F. Abraham, J. C. Boivin, G. Mairesse and G. Nowogrocki, *Solid State Ionics*, 1990, **40–41**, 934–937.

29 F. Abraham, M. F. Debreuille-Gresse, G. Mairesse and G. Nowogrocki, *Solid State Ionics*, 1988, **28–30**, 529–532.

30 T. Iharada, A. Hammouche, J. Fouletier, M. Kleitz, J. C. Boivin and G. Mairesse, *Solid State Ionics*, 1991, **48**, 257–265.

31 M. Guillodo, J. Fouletier, L. Dessemond and P. Del Gallo, *Electrochim. Acta*, 2002, **47**, 2809–2815.

32 M. C. Steil, F. Ratajczak, E. Capoen, C. Pirovano, R. N. Vannier and G. Mairesse, *Solid State Ionics*, 2005, **176**, 2305–2312.

33 J. C. Boivin, C. Pirovano, G. Nowogrocki, G. Mairesse, P. Labrune and G. Lagrange, *Solid State Ionics*, 1998, **113–115**, 639–651.

34 M. H. Paydar, A. M. Hadian and G. Fafilek, *J. Mater. Sci.*, 2006, **41**, 1953–1957.

35 C. Sant and J. P. Contour, *J. Cryst. Growth*, 1995, **153**, 63–67.

36 K. Trzciński, J. Gasiorowski, A. Borowska-Centkowska, M. Szkoda, M. Sawczak, K. Hingerl, D. R. T. Zahn and A. Lisowska-Oleksiak, *Thin Solid Films*, 2017, **638**, 251–257.

37 A. Ojeda-G-P, C. W. Schneider, M. Döbeli, T. Lippert and A. Wokaun, *J. Appl. Phys.*, 2017, **121**, 135306.

38 S. Amoruso, in *Metal Oxide-Based Thin Film Structures*, Elsevier, 2018, pp. 133–160.

39 A. Ojeda-G-P, C. W. Schneider, M. Döbeli, T. Lippert and A. Wokaun, *Appl. Surf. Sci.*, 2016, **389**, 126–134.

40 S. Havelia, S. Wang, M. Skowronski and P. A. Salvador, *J. Appl. Phys.*, 2009, **106**, 123509.

41 R. L. Frost, D. A. Henry, M. L. Weier and W. Martens, *J. Raman Spectrosc.*, 2006, **37**, 722–732.

42 R. Bacewicz and P. Kurek, *Solid State Ionics*, 2000, **127**, 151–156.

43 S. Kumar and P. D. Sahare, *Nano*, 2012, **08**, 1350007.

44 G. Chiodelli, L. Malavasi, V. Massarotti, P. Mustarelli and E. Quartarone, *Solid State Ionics*, 2005, **176**, 1505–1512.

45 J. L. M. Rupp and L. J. Gauckler, *Solid State Ionics*, 2006, **177**, 2513–2518.

46 J. H. Joo and G. M. Choi, *Solid State Ionics*, 2006, **177**, 1053–1057.

47 P. Kurek, J. R. Dygas and M. W. Breiter, *Solid State Phenom.*, 1994, **39–40**, 247–250.

48 E. Pernot, M. Anne, M. Bacmann, P. Strobel, J. Fouletier, R. N. Vannier, G. Mairesse, F. Abraham and G. Nowogrocki, *Solid State Ionics*, 1994, **70–71**, 259–263.

49 N. P. Brandon, S. Skinner and B. C. H. Steele, *Annu. Rev. Mater. Res.*, 2003, **33**, 183–213.

50 K. Momma and F. Izumi, *J. Appl. Crystallogr.*, 2011, **44**, 1272–1276.

25778 | *J. Mater. Chem. A*, 2019, **7**, 25772–25778

This journal is © The Royal Society of Chemistry 2019